J Mater Sci (2019) 54:3421–3437

Metals

Optimization of a dissimilar platinum to niobium microresistance weld: a structure–processing–property study

Daniel Sorensen[1,2,*], Jason C. Myers[3], Bernard Li[1], Wei Zhang[2], Eric Hintsala[4], Douglas Stauffer[4], and Antonio. J. Ramirez[2]

[1] Medtronic PLC, Minneapolis, MN 55432, USA
[2] Welding Engineering Program, Department of Materials Science and Engineering, Ohio State University, Columbus, OH 43221, USA
[3] University of Minnesota Characterization Facility, Minneapolis, MN 55455, USA
[4] Bruker, Eden Prairie, MN 55344, USA

Received: 7 May 2018
Accepted: 11 October 2018
Published online: 22 October 2018

ABSTRACT

Dissimilar metal resistance spot welds, critical to the manufacture of medical devices, typically form brittle intermetallic compounds that are prone to failure. Here, a case study of biocompatible metals platinum and niobium using advanced analytical techniques is presented. It describes the variation of properties and microstructure using microresistance spot welding under four conditions, including a legacy process and processing conditions optimized by design of experiments. Adjustments to the electrode force, welding current, surface roughness, and pulse duration and exchanging the platinum anode contact for a cathode result in a joint with less porosity and greater uniformity in the thickness, chemistry, and microstructure of the fusion zone. The optimized microstructure contains fewer defects, with increased plasticity under deformation and a more uniform microstructure reducing the propensity for failure and variability between welds. Extensive analysis with optical, scanning electron, transmission electron microscopy coupled with nano- and micromechanical testing (such as micropillar compression) was used to characterize the weld zone.

Introduction

The requirements for performance in the medical device industry—especially for materials, components, and devices with long-term human implant applications—are stringent as the devices often provide life-sustaining therapies [1]. Excellent fatigue properties, high fracture toughness, corrosion resistance, high electrical conductivity, high temperature stability, and biocompatibility are but a small list of

Address correspondence to E-mail: dsorensen89@hotmail.com

https://doi.org/10.1007/s10853-018-3018-5

requirements that must be considered when selecting materials for use in medical devices [2]. The list of requirements above often limits the choices for material selections to less commonly utilized and researched materials, especially metals and alloys. The metallic materials infrequently used in industrial applications but routinely used in the medical device industry include MP35N (a nickel–cobalt base alloy), niobium, tantalum, tungsten, β-titanium alloys, platinum, iridium, and gold [3].

The limited material selection options are often coupled with requirements that the materials are joined for medical device component applications. This can result in a situation where dissimilar metal joining is unavoidable. In many cases, fusion welding dissimilar metals is known to form intermetallic compounds (IMCs) in the weld zone [4–6]. The phase diagrams for many of these binary systems contain large numbers of IMCs with low-symmetry crystal systems, making mechanically robust joints difficult to produce [7]. The structure and morphology of these IMCs may vary from weld to weld due to a limited ability to control the fusion zone chemistry [5, 6].

Microresistance spot welding is commonly used in medical devices to join electrical contacts inside of pacemakers, defibrillator, implantable pulse generators, and therapy delivery leads. Previous studies on microresistance welding of fine wires have been performed including β titanium alloys [8], stainless steel to platinum and platinum–iridium [9, 10], nickel [11, 12], and stainless steel [13]. To the authors' knowledge, no research on the subject of joining niobium to platinum has been published.

The equilibrium platinum–niobium system contains many possible IMCs [14], many of which have low-symmetry crystal structures and limited information on their microstructure/properties relationships. The material selection of niobium and platinum, while unconventional, was driven by application-specific requirements for the components. For implant applications, the first requirement for a material is biocompatibility. Both niobium and platinum are known to be biocompatible and biostable [15–17] and are widely used in medical device applications. For this particular application, niobium wire was selected for its electrical properties and corrosion resistance. In addition, melting point/high temperature stability was another requirement for component manufacturing and processing operations which occur at elevated temperatures. Platinum was selected for the second wire because the application required extreme corrosion resistance and high electrical conductivity. These unique design requirements are not uncommon in the medical device industry and have necessitated the use of less common materials along with methods to create and characterize robust welds between them. Moreover, due to a lack of peer-reviewed scientific literature, a detailed characterization of the processing–microstructure–properties relationship for unique welds is required during product development to ensure patient safety, robustness to extreme use conditions, repeatability, and high process capability.

The focus of this study was to optimize and characterize a dissimilar platinum to niobium resistance spot weld starting from baseline joining parameters designated as Condition A. The baseline weld parameters remained the same, but the polarity of the weld was switched by changing the wire on the positive electrode from platinum to niobium and these joints are labeled as Condition B parts. A possible error state when parts are welded by hand includes switching the polarity of the wires. Condition C parts were welded using parameters optimized from a designed experiment. Condition D parts correspond to parts welded using the optimized weld settings of Condition C but a different lot of niobium wire which had a lower surface roughness. This is a possible source of variation in the process and was investigated to see how this possible variable alters the microstructure and properties of the optimized joint.

Experimental

Niobium and platinum wire samples were obtained from commercial sources, and the wires were used in subsequent manufacturing processes to create their higher-level components so they experienced the same processing conditions as a real part. This included general handling, high temperatures, polymer coating, and cleaning processes. The chemical composition measured by inductively coupled plasma–optical emission spectroscopy (ICP–OES) for each sample is listed in Table 1.

The welds selected for comparison in this study are representative of a baseline welding process before and after a design of experiments (DOE) study. The

Table 1 Elemental composition of platinum and niobium samples

Sample	Nb	Pt	Hf	C	H	N	O	Ru
Niobium wire A	Balance	N/A	0.011	0.0083	0.0001	0.0037	0.0093	N/A
Niobium wire B	Balance	N/A	0.011	0.0011	0.0004	0.0042	0.0086	N/A
Platinum wire	NT	Balance	NT	NT	NT	NT	NT	0.0074

Values are in wt%

NT stands for not tested

Table 2 Welding parameters used for this study

Condition	Electrode polarity	Current (kA)	Electrode force (N)	Niobium surface roughness (Ra, nm)	Weld duration upslope/hold/downslope (ms)
A	Pt on (–) electrode	0.50	13.34	938.0 (Wire A)	25/22/2
B	Pt on (+) electrode	0.50	13.34	938.0 (Wire A)	25/22/2
C	Pt on (+) electrode	0.43	14.01	938.0 (Wire A)	3/2/0
D	Pt on (+) electrode	0.43	14.01	357.6 (Wire B)	3/2/0

DOE performed was a traditional full factorial four-factor, two-level experiment. The experimental factors were welding current, electrode force, upslope time, and hold time. The width of the interface, pull force, and qualitative scores of interfacial porosity were used as responses. After execution of the DOE, the results were analyzed, and the weld schedule was optimized for weld width and pull strength using Minitab 16 commercial statistical analysis software response optimizer. The samples are designated by weld Conditions A–D listed in Table 2 with their welding parameters. All welds were performed using a Miyachi Unitek Model 1-284-01 resistance welder with class II copper electrodes in the opposed configuration.

All samples were mounted for metallographic preparation with the niobium wire in the longitudinal direction and the platinum wire in the transverse direction. All samples were mounted in ProbeMet conductive mounting media, ground to the center of the niobium wire, and prepared using standard metallographic techniques [18] followed by a vibratory polish to remove residual surface deformation. All cross-sectioned joints were imaged with a Zeiss Axiovert Observer A1M metallographic microscope to visualize the morphology of the welds.

Samples for transmission electron microscopy and micropillar compression experiments were fabricated on FEI Versa and Scios DualBeam instrument equipped with an FEI EasyLift system. Foils for transmission electron microscopy were lifted out from the center of the weld zone, rotated 90°, and thinned with 30 kV Ga^+ ions to a thickness of 100 nm. They were finally thinned to electron transparency with an ion beam accelerating voltage of 5 kV.

Conventional and analytical transmission electron microscopy (TEM) was performed using an FEI Tecnai G^2 F30 Schottky field-emission gun (FEG) TEM operating at 300 kV, equipped with an EDAX X-ray detector or an FEI Titan G2 60-300 probe-corrected FEG STEM equipped with an X-FEG high-brightness electron source, ChemiSTEM EDS detectors, and Gatan Enfinium EELS spectrometer. The semiquantitative EDS measurements recorded during this study, while repeatable from day to day and sample to sample, were obtained from dissimilar metal weld samples with unknown chemistries, and there is no available platinum–niobium alloy standard in the open literature to calibrate to.

Nanoindentation testing was performed using a Hysitron TI-950 Triboindenter in displacement-controlled mode with a 90° cube corner probe. The area function was calculated prior to testing, and at the start and end of each day testing occurred, the hardness and reduced modulus of the fused quartz standard were verified at the displacement depth tested (for this study, 50 nm) to ensure the tip geometry from the previously calculated area function had not changed during testing. All analysis was performed using a load function with a 5 s load to

peak displacement, a 2 s hold, and 5 s unloading segment.

Lastly, micropillar samples of the weld zone and base materials were fabricated using annular milling techniques at 30 kV using a 15 nA probe current for rough cutting and progressively smaller probe currents down to 50 pA for final polishing. Pillar diameters were approximately 5 μm with a taper angle of less than 5°. All pillars were fabricated from metallographic cross-sectioned parts using an FEI Versa or Scios DualBeam. The compression experiments were performed using a conical probe polished to a 10-μm flat punch on a Hysitron TI 980 Triboindenter fitted with a MultiRange NanoProbe. All compression testing was performed using a loading rate of 20 nm/s and a displacement to approximately 10% global strain. Following the compression experiments, the samples were prepared for TEM analysis using the methods listed above.

In resistance spot welding, the transient temperature distribution, due to Joule heating, is essential to help understand the weld nugget initiation and growth. However, the small geometry to be joined and the rapid welding cycle made it difficult (if not impossible) to measure the temperature distribution in the weld experimentally. Hence, a three-dimensional (3-D), transient finite element model was developed using Abaqus CAE based on fully coupled thermo-electro-mechanical simulation that accounted for the electrical contact resistance at the interfaces [19]. The simulation was limited to the initial stage when the current was ramped up. Simulation beyond the initial stage encountered numerical divergences issue as the mesh became overly distorted. Nevertheless, the calculated temperature history during the initial stage still provided useful information to understand the effect of welding process parameters on the joint formation, as described later in Section E of the Results portion of the paper.

Results and discussion

Macro- and microstructure analysis

Following the welding process, all joints maintained a shiny metallic silver color, signifying a lack of oxidation, with only small amounts of expulsion observed. The platinum wire was embedded into the niobium wire which can be seen in inset of Fig. 1d. The lack of visual weld quality indicators such as large-scale melting, a visual weld nugget, or high levels of expulsion required the joints be investigated further. Careful cross sections of each weld condition gave more insight into the joint quality.

Representative optical metallographic cross sections seen in Fig. 1 show varying levels of expulsion and platinum wire embedment that are expected to change as the welding conditions are modified. Figure 1d inset shows a low-magnification image of a platinum to niobium cross-wire weld for the reader's reference. The cross sections revealed the wires were bonded due to the continuous interface, but no evidence of material mixing or local recrystallization could be resolved using light microscopy, leaving the character of the bond (mechanical, solid state, fusion) unknown.

Further analysis using a focused ion beam, shown in Fig. 2, to make site-specific cross sections and TEM samples showed Condition A welds contained large amounts of porosity. This porosity was significantly reduced or eliminated in Condition B (and C/D) by changing the electrode polarity. Simultaneously, the microstructure became more uniform and the interfacial region of the weld became wider. The channeling contrast allowed some microstructural and morphology information to be ascertained but the spatial resolution of EDS in the SEM is insufficient to characterize the multilayered weld interface.

Conventional bright-field TEM imaging of welds fabricated from each of the four processing conditions showed an array of microstructures and morphologies in the interfacial region that varied between welding conditions. Representative BF-TEM images of each welding condition are shown in Fig. 3. Samples from Condition A were found to have the thinnest interfacial layer, on the order of 300 nm, and contain large amounts of porosity at the platinum–weld interface. Randomly distributed niobium-rich regions—seen as small, globular, and dark regions in BF-TEM images—were also observed in parts joined using Condition A, as shown in Fig. 3a. Parts welded using a Condition B schedule had a similar microstructure to Condition A parts with the notable differences of a wider weld zone, oftentimes reaching 1 μm across, less porosity, and larger areas with niobium-rich globules observed (see Fig. 3b). The increase in weld zone thickness following reversal of electrode polarity may be a result from local heating changes due to the Peltier effect where

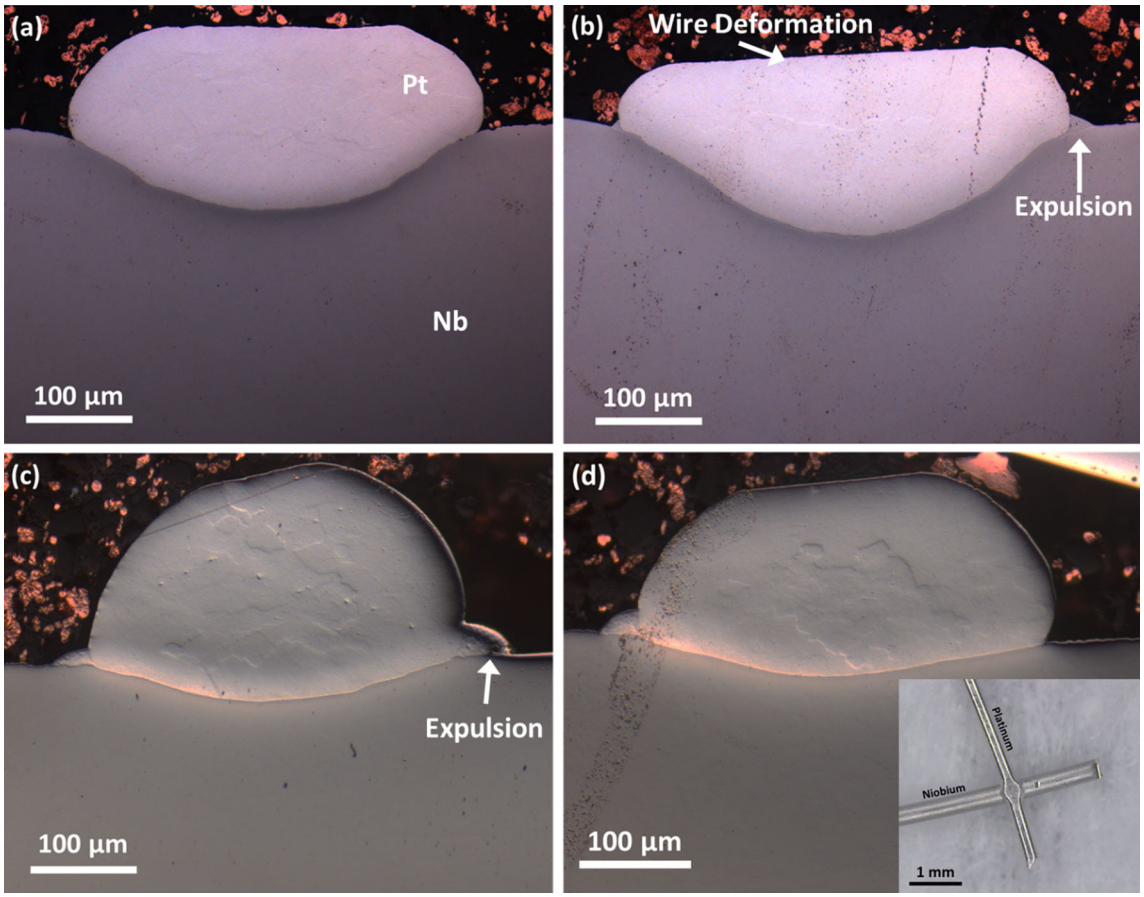

Figure 1 Metallographic cross-sectional images of Pt–Nb resistance welds joined using **a** Condition A processing parameters where severe deformation to the platinum wire has occurred and no expulsion is visible. **b** Condition B again showing large amounts of plastic deformation in the platinum wire but with small amounts of expulsion observed. **c** Condition C showing much less embedment and deformation of the platinum wire into the niobium wire with large quantities of weld expulsion. **d** Condition D showing moderate amounts of platinum deformation, embedment, and small amounts of expulsion. Inset in (**d**), an optical micrograph showing the as-joined cross-wire microresistance weld.

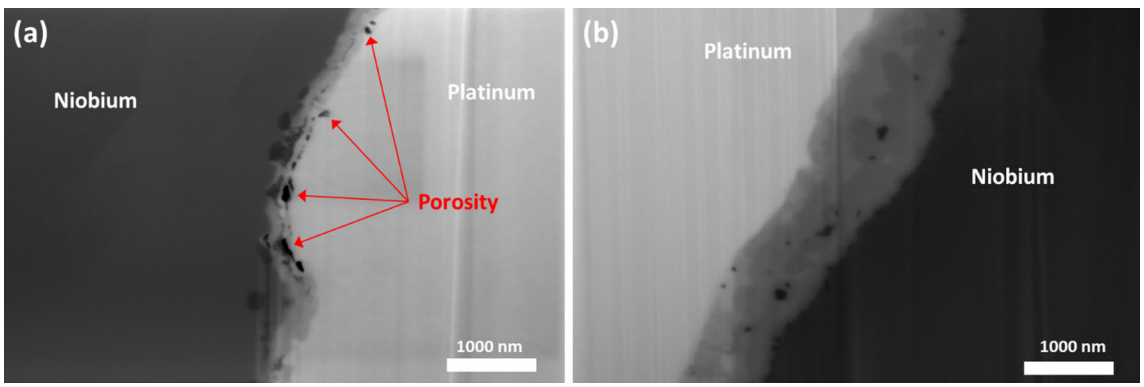

Figure 2 FIB cross section of **a** Condition A weld with porosity on the platinum side of the weld interface shown. **b** FIB cross section of a Condition B weld joined with the same weld parameters as (**a**) but the electrode polarity was reversed.

more heat at one interface is generated depending on the current path during the welding cycle [20–23]. In dissimilar metal welds and joints with high-resistance work pieces of differing thickness, the Peltier effect can be used to control the weld nugget size and location. In addition, the wider weld zones

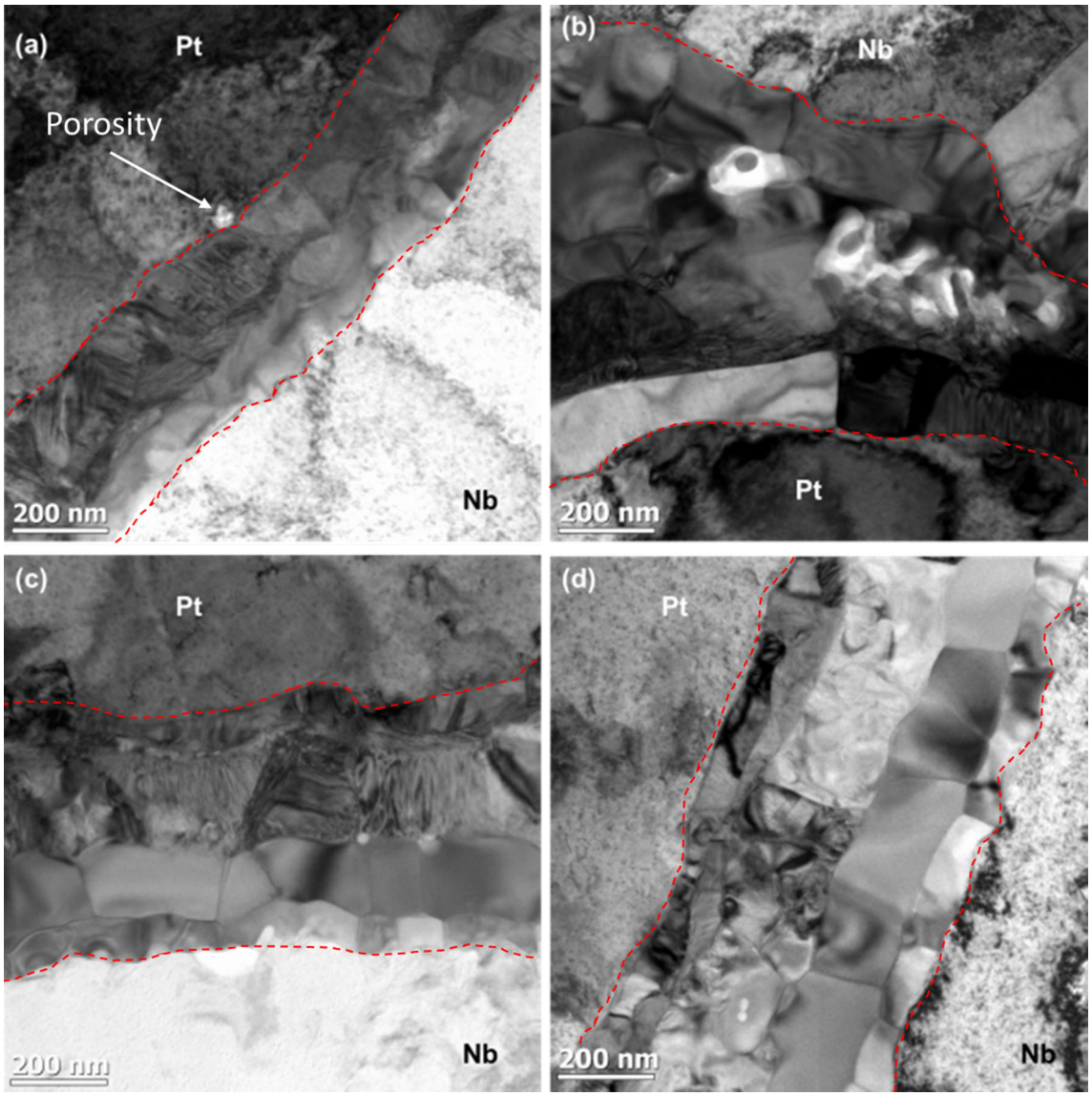

Figure 3 Representative BF-TEM images of Pt–Nb resistance welds (with weld zones highlighted by red dotted lines): **a** Condition A processing parameters. A pore (white circle) can be seen at the platinum–weld zone interface. **b** Condition B showing non-uniform interface morphology and niobium-rich regions (dark globular features surrounded by white). **c** Condition C showing a more uniform interfacial region with five distinct phases. **d** Condition D showing a similar microstructure to Condition C but with thicker platinum-rich phases observed.

signify a larger melted region which may solidify more slowly, thus allowing more time for trapped gasses to escape. On the other hand, a small weld zone may solidify very quickly, trapping gasses as porosity as seen in Fig. 2.

The optimized weld was designed with the intent to lower the weld temperature and obtain more repeatable microstructures and therefore properties. By decreasing the welding time (t) and peak welding current (I) and increasing the force [thus decreasing the contact resistance (R)], the total energy input (Q) to the weld was decreased as shown in Eq. 1.

$$Q = I^2Rt \tag{1}$$

The resulting weld, Condition C, had a marked increase in weld width, and a much more uniform microstructure in terms number of phases present, thickness of each phase, and thickness of each interface (see Fig. 3c) compared to Conditions A and B. The high energy input used to join Conditions A and

B resulted in inconsistent weld zone widths, globular regions of nearly pure niobium observed in the weld, and different numbers of intermetallic phases in the joint as shown in Fig. 3a–b. No porosity was observed, and only small spherical niobium-rich particles were observed in the weld zone. The two phases closest to the niobium base material consisted of small grains with diameters on the order of 50–100 nm. The phase in the center was found to have a grain size of approximately 200 nm and was confirmed by high-resolution transmission electron microscopy (HRTEM) imaging to be heavily faulted. The two phases closest to the platinum base material also contained stacking faults but these phases had smaller grain sizes ranging from 20 to 50 nm in thickness and a flat "pancake"-type morphology. While the local heating was decreased using welding parameters of Condition C, reducing the contact resistance further was of further interest. As the welding parameters had been optimized from the designed experiments, a common noise variable that is not traditionally controlled but is important nonetheless was the surface roughness of the workpieces. Similar to electrode force, the larger number of contact spots at the welding interface (smoother surface) decreases the contact resistance [24]. The surface roughness was investigated in two different conditions: Wire A with a surface roughness of 938.0 nm (as in Condition C) and Wire B with a surface roughness of 357.6 nm (as in Condition D).

Lastly, Condition D welds were found to lack porosity and have the most uniform microstructure, weld zone thickness, and phase morphology, as shown in Fig. 3d. The morphology and average grain size were found to be like the weld zone of Condition C joints. Condition D samples were welded using the same force, time, and current parameters but the niobium wire had a lower surface roughness by roughly a factor of three, decreasing the contact resistance.

It is noted that the weld nugget size of a resistance spot weld generally increases with the welding heat input. Hence, the thicker weld zone for Conditions C and D, made at a much lower heat input than Condition A, might seem counterintuitive. As mentioned previously, Fig. 1a and b reveals a much more severely deformed platinum wire as well as a much deeper embedment into the niobium wire for Conditions A and B than Conditions C and D. This suggests that the joints in the former two conditions were significantly hotter than those in the latter, consistent with the heat input used. It is postulated that the weld zone was stretched as the platinum wire was pressed deep into the niobium wire, resulting in an inconsistent and thin weld zone in Condition A. The temperature distribution during welding is explained using the finite element analysis results later in this section.

High-angle annular dark-field scanning transmission electron microscopy (HAADF-STEM) was performed to qualitatively image using atomic number (Z) contrast. The HAADF images, shown in Fig. 4, reveal a gradual change in contrast as the weld zone moves from the niobium base material to the platinum base material. HAADF imaging also revealed all phases nearest the niobium base material contained fine globules which decreased in concentration as the Pt base material is approached. High-resolution STEM imaging at the interface between regions 2 and 3 revealed the globules to be approximately 3 nm in diameter, niobium rich, and randomly dispersed in the weld zone as seen in Fig. 5. These smaller niobium-rich particles were observed in all weld conditions to some extent and were similar in size. The particles were not observed to cross-phase boundaries in any weld condition investigated in this study. Changing the energy input from weld Conditions A and B to Conditions C and D revealed the concentration of niobium-rich particles of varying sizes decreased as energy input was lowered. This suggests the amount of niobium base material melting is highest in Conditions A and B. The large (50–100 nm)-sized globules randomly distributed within welds processed using Conditions A and B suggest that, upon solidification, the solubility limit of niobium in the phases that form in the weld zone decreases enough that excess solute is expelled from the crystal and agglomerates into niobium-rich regions. This observation also suggests the energy input to Conditions A and B welds is higher. Niobium has a heat of fusion nearly 25% higher than platinum [25], and the large niobium-rich regions in the weld signify Conditions A and B welds had high temperatures local to the niobium side of the joint. As the energy input was decreased, the number and size of niobium-rich globules decreased dramatically. Conditions C and D welds contained very few larger particles, although representative examples are seen in Fig. 3c–d as white globular features, 25–50 nm in diameter. As mentioned in the above, all conditions

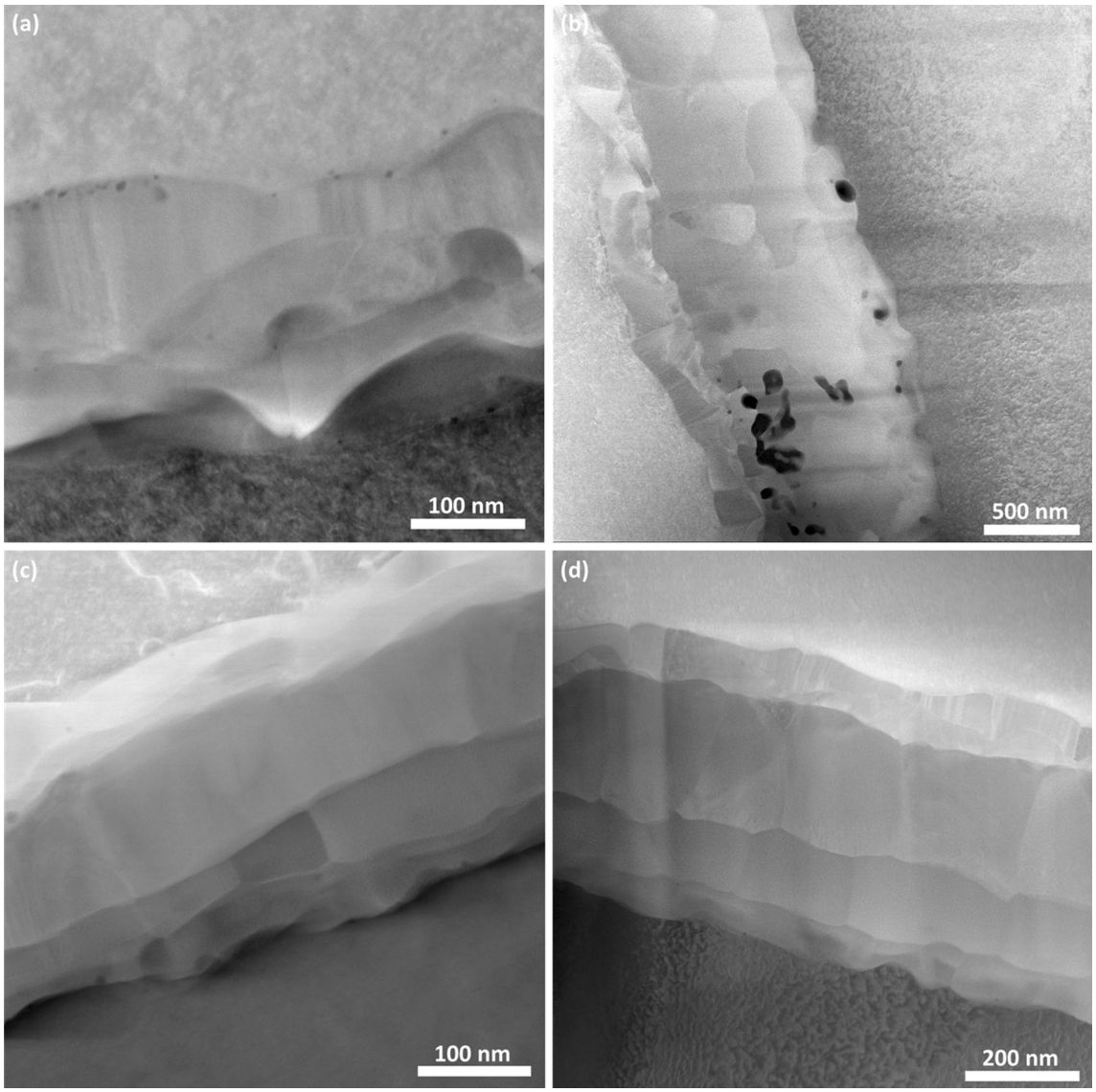

Figure 4 Representative HAADF-STEM images of Pt–Nb resistance welds: **a** Condition A processing parameters. **b** Condition B showing non-uniform interface morphology and niobium-rich regions (seen as dark globular features). **c** Condition C showing a more uniform interfacial region with five distinct phases. **d** Condition D showing a similar microstructure to Condition C but with thicker platinum-rich phases observed. The darker contrast regions in each image are the niobium base material.

contain 3–5-nm-diameter niobium-rich particles. These particles are more densely in the niobium-rich regions of the welds and decrease as phases approach the platinum base material, as shown in Fig. 5. This observation suggests upon melting the weld zone was supersaturated with niobium which precipitated out of solution as the weld solidified.

Chemical analysis

Characterization of the chemistry across the platinum–niobium resistance weld interface is critical for an understanding of the effects of weld process parameters on the microstructure and mechanical properties of the resulting joint. In this study, STEM-EDS scans were acquired from each of the distinct interfacial zones found in each of the samples joined with unique processing conditions. The semiquantitative EDS results, shown together in Fig. 6a and

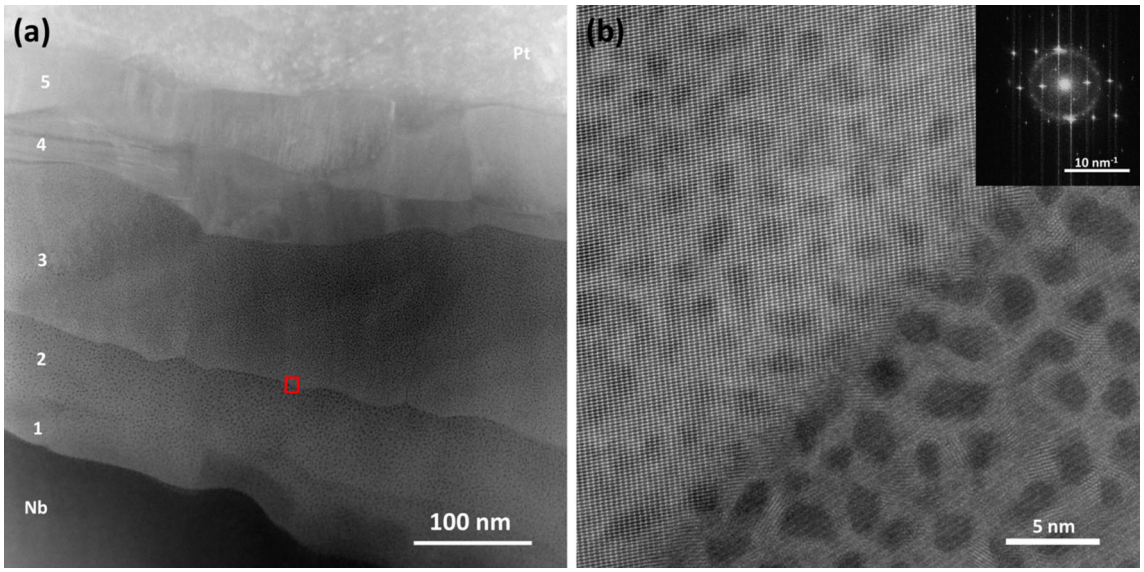

Figure 5 **a** Condition C HAADF-STEM image showing the five distinct phases observed in the platinum–niobium resistance weld interface and analyzed by STEM EDS and EELS. **b** Atomic resolution image of the interface between regions 2 and 3, shown by rectangle in Fig. 5a. The Nb-rich particles are dispersed randomly in the crystalline matrix.

tabulated in Table 3, show the chemistry in each layer to be consistent between all processing conditions. However, Condition D was found to have statistically lower niobium/higher platinum concentrations in region 1 and higher niobium/lower platinum concentrations in region 3. Variation in the STEM-EDS analysis can be caused by diffraction effects, sample thickness [26], or overlap between phases within the sample thickness. This means this statistical signal may not be practically significant. The EDS analysis of all resistance weld conditions showed one major departure from the general five-layer structure observed in Conditions B–D. The phase second closest to the niobium base material was absent in all samples of Condition A analyzed. The non-uniformity of both weld zone thickness and the width of individual phases made the semiquantitative EDS analysis more repeatable if line scans were collected within the individual regions in the joint instead of across the entire weld zone.

Identification of the individual phases in each weld condition using traditional methods including convergent beam, selected area, and nanodiffraction experiments was unsuccessful. The fine grain sizes, proximity to different phase regions, and apparent low symmetry of the crystals made a positive identification using electron diffraction techniques challenging. The inability to positively identify the phases leaves uncertainty in the EDS results. Furthermore, the chemistries measured by EDS in each region of the weld zone often times were found to be in different phase fields on the platinum–niobium equilibrium phase diagram [14]. Given the non-equilibrium nature of these microresistance weld processes, the measured chemistries may not be found in the equilibrium phase diagram. A second analytical method to characterize these phases was required to verify the EDS results. The sensitivity of low (plasmon)-loss electron spectroscopy to crystal and electronic structure changes [27] made it an appropriate method to qualitatively confirm the regions of similar chemistry and morphology. This technique was helpful to confirm different regions had the same crystal structure when selected area and nanodiffraction methods were unable to identify the individual phases. The overlaid monochromated electron energy loss (EEL) spectra reported in Fig. 6b clearly show each region in the interfacial region has a unique plasmon loss peak energy and shape which signifies different coordination numbers and atomic arrangements [27]. The plasmon loss peak energies for each region in the weld zone and base materials are plotted together in Fig. 6c for Conditions A–D. The data revealed all regions have statistically similar plasmon loss energies between welding conditions. This result leads to the conclusion that the outlier EDS data (i.e., region 3) for Condition D welds are a test artifact and the phase regions in Condition D

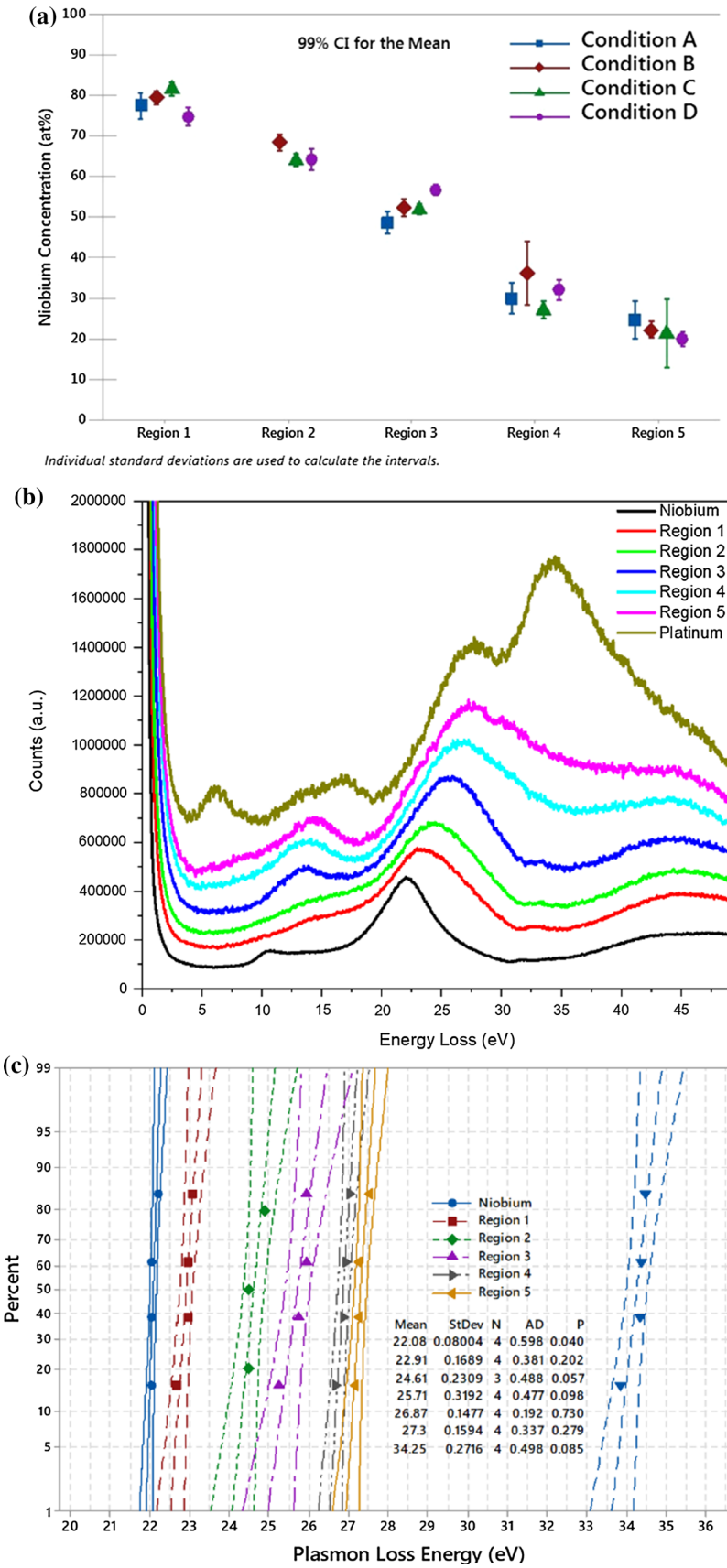

Figure 6 **a** Chemical composition in each region of the Nb–Pt welds across all process conditions measured using STEM-EDS. **b** Overlaid monochromated EELS data showing plasmon peak shapes and shifts in the weld zone and base materials. **c** Probability plot showing distribution of plasmon loss peak energies for each phase and base materials in each weld condition. A representative image showing the individual labeled phases is shown in Fig. 5a.

Table 3 Compositions in atomic percent of each apparent phase of Nb–Pt resistance weld

Condition	Region 1	Region 2	Region 3	Region 4	Region 5
A	$Nb_{0.78}Pt_{0.22}$	Not Present	$Nb_{0.49}Pt_{0.51}$	$Nb_{0.30}Pt_{0.70}$	$Nb_{0.25}Pt_{0.75}$
B	$Nb_{0.80}Pt_{0.20}$	$Nb_{0.68}Pt_{0.32}$	$Nb_{0.52}Pt_{0.48}$	$Nb_{0.36}Pt_{0.64}$	$Nb_{0.21}Pt_{0.79}$
C	$Nb_{0.82}Pt_{0.18}$	$Nb_{0.64}Pt_{0.36}$	$Nb_{0.52}Pt_{0.48}$	$Nb_{0.27}Pt_{0.73}$	$Nb_{0.21}Pt_{0.79}$
D	$Nb_{0.75}Pt_{0.25}$	$Nb_{0.64}Pt_{0.36}$	$Nb_{0.57}Pt_{0.43}$	$Nb_{0.32}Pt_{0.68}$	$Nb_{0.25}Pt_{0.75}$

Values are the average of EDS line scan data for each sample and region. Note that the outlier EDS data in region 3 for Condition D welds are likely caused by a test artifact, as explained in the text

welds are the same chemically, structurally, and morphologically as those observed in A–C welds.

Mechanical performance

The narrow and often inhomogeneous weld zones observed in the joints studied required the mechanical properties be measured using nanoindentation. The ability of instrumented indentation to measure mechanical properties of site-specific locations [28] was used to characterize the effect of process conditions on mechanical properties in the weld zone. All nanoindentation testing was performed ex situ which required the fusion zone be located by using the indenter in imaging or scanning probe mode and looking for small height variations on the surface consistent with the width of the weld zone. The small grain size, inconsistent weld zone width, and proximity of many of the weld zone phases to the base material required indents to be performed approximately in the center of the interface and assume the plastic zone interacts with most of the phases across the weld zone. Previous studies have demonstrated the sensitivity of hardness and indentation modulus values when measuring samples where dissimilar material interfaces are present [29]. The plastic zone size for a sharp cube corner indenter ranges from $3a$ to $6a$ where a is the radius of curvature of the probe [30]. The cube corner used for this analysis had a radius of curvature of $\sim$ 50 nm making the plastic zone size underneath the indent at least 150 nm. For the above reasons, all hardness and indentation modulus values are considered a composite hardness of the weld instead of being reported as phase specific. The results of the nanoindentation experiments are summarized as box–whisker plots shown in Fig. 7 which also shows the representative test locations. The results show consistent hardness values in the weld zone of Conditions A–C with average values of approximately 11 GPa. The indent locations where the highest hardness outlier data points ($\sim$ 17 GPa) were collected in Conditions A and B corresponded to niobium-rich regions as seen in the HAADF-STEM images in Fig. 4b and confirmed with STEM-EDS and backscattered SEM imaging. STEM imaging shows the large niobium-rich phases to have a nanograined lamellar structure which could partially explain the higher hardness values recorded at these locations.

Regions of fusion welds with localized high hardness may act as stress risers or crack initiation sites and should be avoided if possible [5, 6]. The average hardness value in Condition C was comparable to Conditions A and B but the more uniform microstructure and slightly wider weld zone in Condition C resulted in a lower standard deviation in the dataset. The general microstructures observed in Figs. 3 and 4 showed all four processing conditions yielded welds with slightly different morphologies but the same layered microstructure. Condition D was found to have hardness values nearly 3 GPa lower than Conditions A–C. The indentation modulus values in all welding conditions ranged from 170 to 250 GPa; in all cases, the weld zone indentation modulus was found to be higher than the platinum base material.

Investigation of the mechanical properties of the weld zone using nanoindentation and a cube corner probe was unable to resolve phase-specific mechanical properties but nonetheless gave insight into the mechanical and elastic properties of the weld zone as a composite. The hardness values of Conditions A–C were found to be a factor of five larger than the base materials. This result is not surprising considering the discussion above related to microstructure, morphology, and chemistry of the welds. All joints are multiphase and nanograined and contain niobium-rich precipitates which separately could be responsible for incremental strengthening of the weld zone compared to the base material. The effects of orientation and residual stress were not considered but

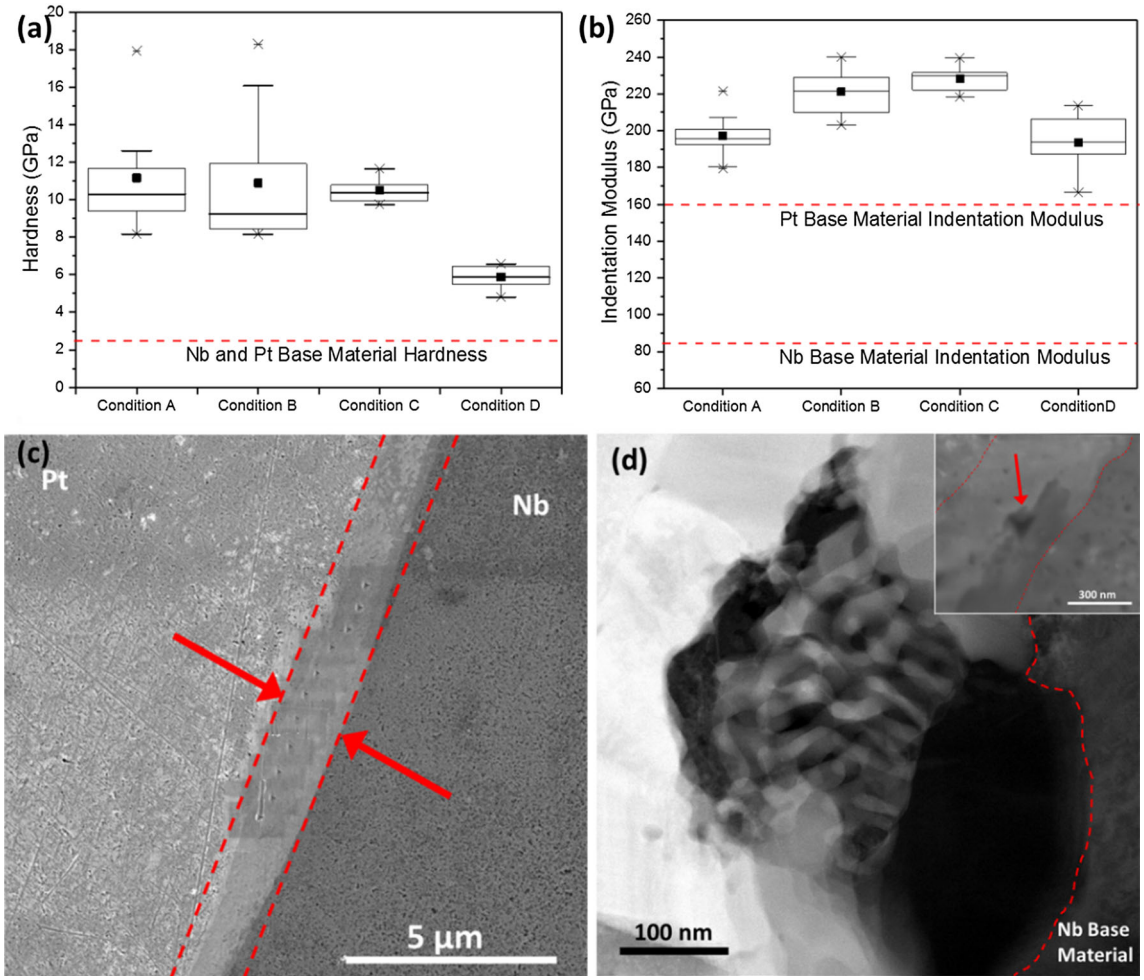

Figure 7 Box and whisker plots summarizing the results of nanoindentation testing for **a** hardness and **b** indentation modulus. **c** Backscattered electron micrograph showing a representative microstructure of a platinum–niobium resistance weld and the test locations for nanoindentation. The dotted line signifies the approximate weld zone boundaries with the base materials. **d** BF-TEM image of a niobium-rich globular feature found in a Condition A weld that resulted in localized high hardness values. SEM image of a Berkovich indent on one of the niobium-rich globules that had a high hardness value seen in inset of (**d**). The dotted red lines in the box plots referencing the base material properties were measured using nanoindentation.

may have a small effect on the resulting hardness as well.

Together, these proposed strengthening mechanisms result in the high hardness values recorded in the weld zones. The hardness values measured in the weld zone of Condition D joints had values between the base materials and weld zones in Conditions A–C. This discrepancy can be attributed to differences in weld zone widths and individual phase thicknesses within the interfacial regions of different weld conditions. The location of the indents for each weld was confirmed using SEM. The lower hardness values and tighter distributions for Condition D welds can be attributed to indentation test locations being localized near the center of the weld and phase region 3. Condition A–C welds had less uniform morphologies and had thinner weld zones, making it likely hardness information from phases near the base materials was included in the composite hardness values.

The composite indentation modulus values followed a different trend than hardness. The indentation modulus values of Condition A and D were statistically similar, as were those of Conditions B and C. Inspection of the samples following indentation experiments provided evidence that the two distributions of indentation modulus recorded for this work were a result of the random location of the

indent in each weld, the phases that elastically deformed, and if the indent was centered on an individual phase or phase interfaces. The spread in indentation modulus values from ex situ testing is a direct result of limited material and disconnect between phase identification and test locations. At the expense of throughput, further experiments using in situ techniques could be used in the future to measure phase-specific mechanical and elastic properties.

As previously discussed, the small dimensions and cross-wire geometry of the weld make testing the actual mechanical properties of the joint difficult. Furthermore, the base materials are fully annealed because of previous processing steps, making all attempts at tension or pull testing fail in the base material. While pull testing demonstrates the weld is stronger than the base materials in uniaxial tension or peel, little information on the properties and performance of the actual weld itself is gained.

To better characterize the local response of each weld zone to a severe plastic deformation, micropillar samples were fabricated that included both base materials and the weld zone as shown in Fig. 8a. FIB/SEM analysis of pillars following compression experiments revealed large amounts of the deformation had been accommodated by slip of the much softer base materials as shown in Fig. 8b. FIB cross sections of compressed pillars show severe deformation of the intermetallic layers that did not result in apparent fracture but instead followed the flow patterns of the base material as seen in Fig. 8c.

Following FIB cross sectioning, the compressed samples were lifted out and prepared for TEM analysis. Again, the microstructures of the compressed samples showed much of the deformation was accommodated by the base materials based on large dislocation pileups observed at the base material–weld zone interfaces. The microstructure of Condition A welds following a severe plastic strain showed only signs of heavily faulted intermetallic phases. Few instances of cracking were observed and were only found in areas of heavy deformation as seen in Fig. 9a and c where the weld zone had been bent nearly 90° during the compression testing and a crack appeared to have nucleated from preexisting porosity in the weld. Condition C welds responded similarly to a large compressive strain. Figure 9d–e shows a low-magnification micrograph of a Condition C weld following a 10% compressive strain. Only a single

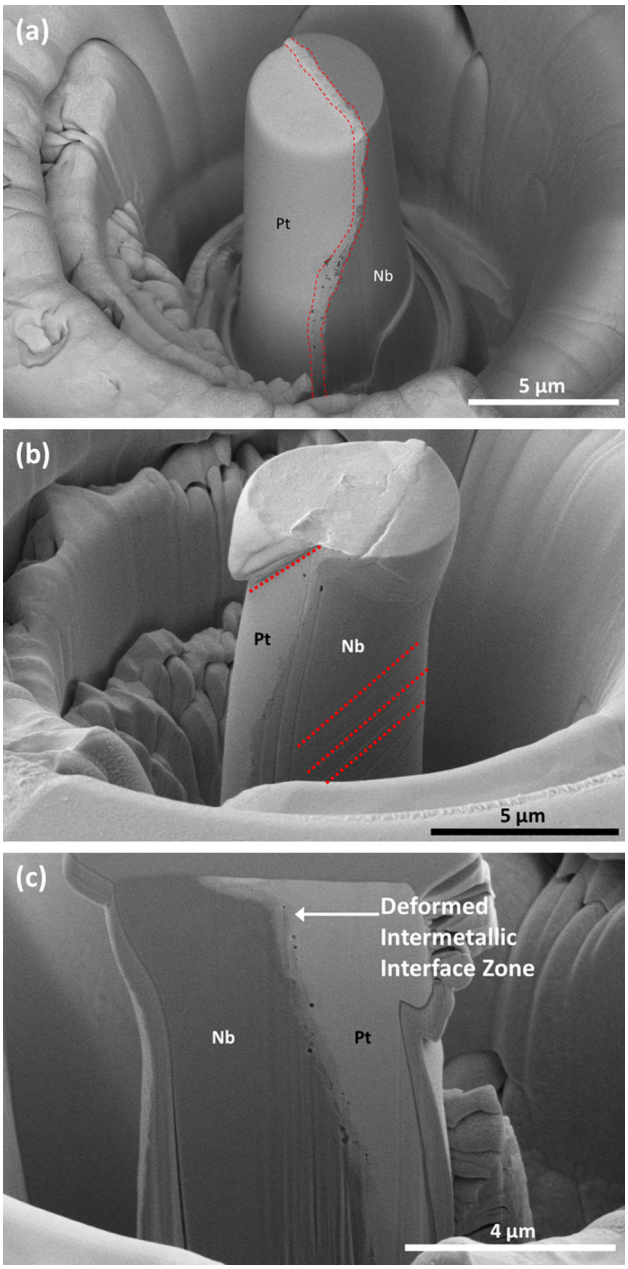

Figure 8 Secondary electron image showing: **a** a representative as-milled pillar with the interfacial layer highlighted by the dotted lines, **b** compressed pillar showing slip in base materials shown by dotted lines, and **c** image of FIB sectioned lamella of deformed pillar prior to lift-out.

intergranular crack was found. As with the deformed welds in Condition A, many of the phases in Condition C weld zones were found to accommodate the strain by forming higher concentrations of stacking faults observed in the platinum-rich phases and highlighted in Fig. 9b. Interestingly, the intermetallic phase labeled as "2" in Fig. 5 was found to contain

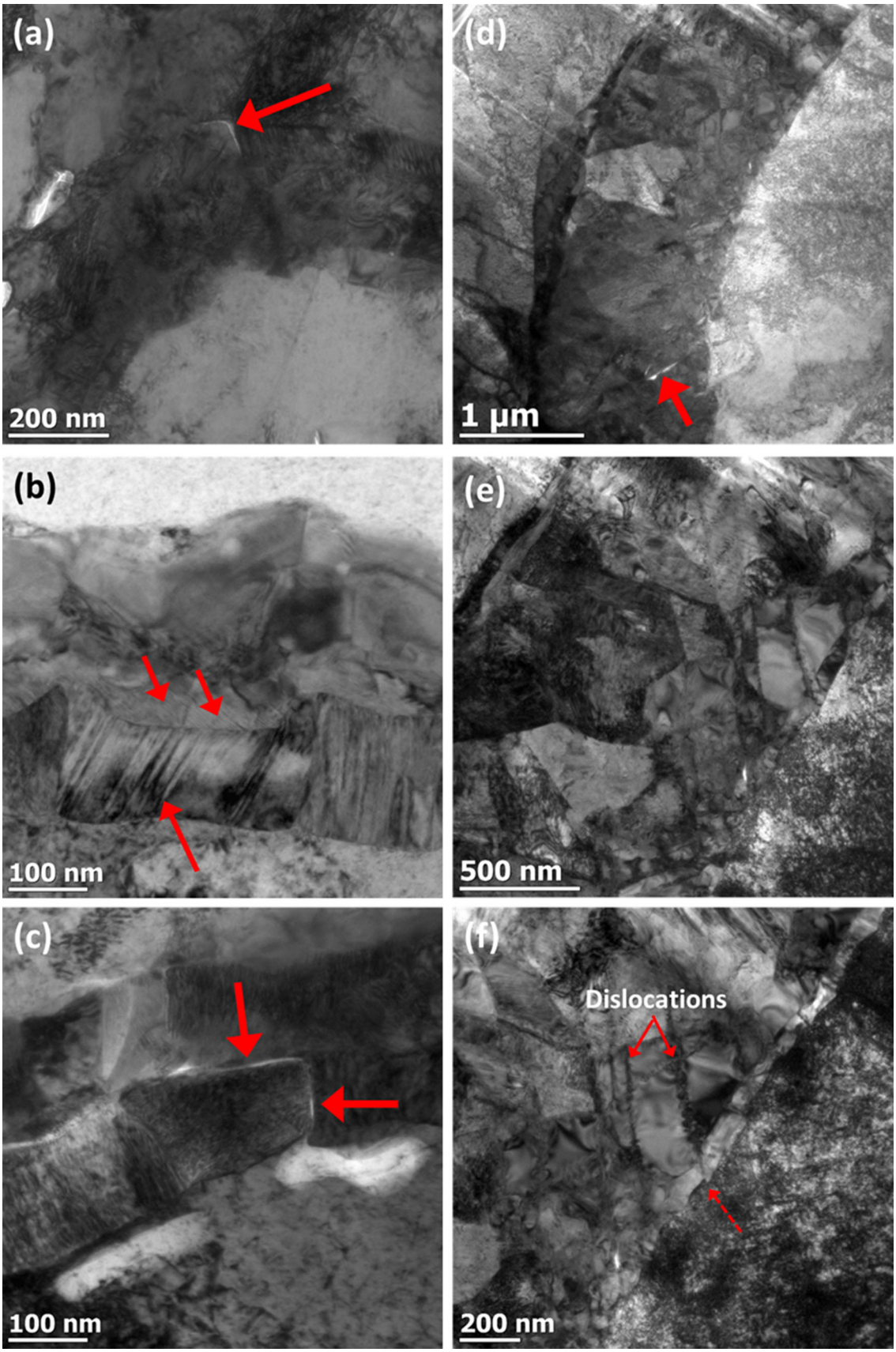
(a)
200 nm
(d)
1 μm
(b)
100 nm
(e)
500 nm
(c)
100 nm
(f)
Dislocations
200 nm

◀**Figure 9** BF-TEM images showing the microstructure of **a**–**c** Condition A and **d**–**f** Condition C following micropillar compression experiments to approximately 10% compressive strain. Interfacial cracks are shown as the solid arrows in (**a**), (**c**), and (**d**). Faulted structures are highlighted in (**b**). Lines of dislocations are highlighted in (**f**) along with the phase sheared by the line of dislocations shown with dotted arrow.

dislocation loops and sub-grain boundaries. In one location, shown in Fig. 9e, the line of dislocation loops was observed to have caused an adjacent phase to shear as the dislocations passed through the phase boundaries into the base material.

The results of micropillar compression testing demonstrated the robustness of these joints under extreme deformation. The findings of the pillar compression testing and postmortem analysis, while qualitative, show the phases in the welds can accommodate large strains by forming additional stacking faults (primarily in the phases adjacent to the platinum base material) or even plastically deforming. These observations significantly reduce the risk of the performance of this joint if used in a condition with mechanical loading.

Finite element modeling

A finite element model was applied to simulate the microresistance spot welding process for Conditions A and C. As the model did not consider the Peltier effect (and thus the electrode polarity), the Joule heating and deformation for Condition A were equivalent to those for Condition B. Condition D was not considered due to a lack of electrical contact resistance between niobium and platinum with a different surface roughness. As mentioned previously, the model was unable to simulate the entire welding cycle due to numerical convergence issue resulting from excessive mesh distortion. Nevertheless, some valuable information from the initial upslope of welding current application for Conditions A versus C was gathered and thus warrants a brief discussion.

As shown in Fig. 10, the finite element results revealed differences in the peak temperature between the workpieces, temperature distribution, and heating rates for Conditions A and C. Note that temperature field was plotted at a current-on time equal to 12 ms for Condition A versus 1.4 ms for Condition C. For the former, the current was ramped up more gradually to the peak current of 0.50 kA over 22 ms. As a result, there was more time for heat conduction, and consequently both base materials were heated significantly. The calculated result for Condition A shows the platinum wire already deformed significantly even at current-on time of 12 ms, which is consistent with the experimental observation of high amounts of collapse in the platinum wire (Fig. 1a). On the other hand, for Condition C, the current was ramped up

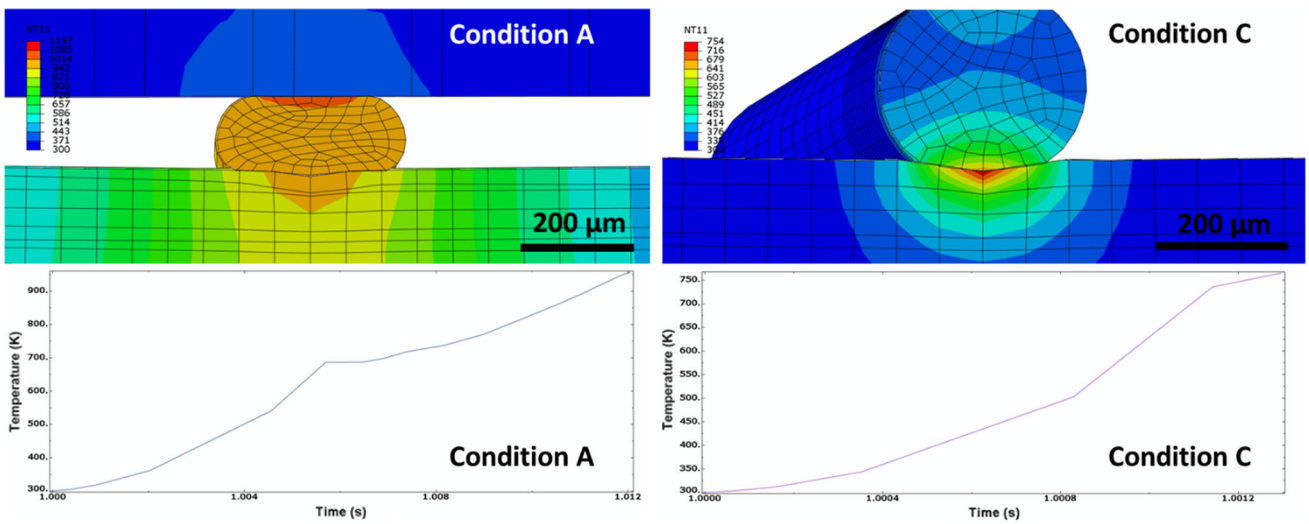

Figure 10 Temperature distribution and deformed shape (top row) along with temperature profiles of a node at the wire interface for Conditions A and C (bottom row). The welding current was switched on at time = 1 s. The simulated current-on time was 12 ms and 1.4 ms for Conditions A and C, respectively.

much more quickly to the peak value of 0.43 kA in only 3 ms. As a result, the heating was mostly intense at the interface between the two wires, and the bulk of wires remained cool.

As the simulation did not proceed beyond the initial upslope, the formation of weld nugget was not predicted. But based on the results in Fig. 10, it is postulated that a melt layer quickly formed at the niobium/platinum interface and the melt layer then grew (or expanded) upon further heating. In Condition C, as the bulk of wires remained cold, the melt layer growth occurred in place. On the other hand, in Condition A, both wires were substantially heated and both wires deformed considerably. As the platinum wire indented further into the niobium wire, the melt layer between the two wires was stretched and thus thinned. If such hypothesis is true, it seems to be consistent with the experimental microstructure analysis where Condition C welds had a larger, more uniform microstructure in the weld zone compared to Condition A welds.

Conclusions

The results of these experiments have shown that a complex microresistance weld that utilizes less common materials can be developed and characterized using designed experiments, nanomechanical testing, analytical electron microscopy, and finite element modeling. The platinum to niobium cross-wire resistance weld studied was improved by reversing the electrode polarity, decreasing the welding current, duration, and electrode force. Welding niobium with a lower surface roughness did not appear to have a large effect on the output other than a qualitatively more uniform weld, making wire surface quality a negligible source of variation. The ability to quickly and efficiently correlate the processing–microstructure–properties relationship using these techniques can burn down significant amounts of design risk, speed up development time, improve product quality, and increase process capability. The advanced characterization tools utilized to study the platinum–niobium welds revealed a robust joint containing intermetallic compounds which plastically deforms was created and could be used for applications requiring high reliability.

Acknowledgements

The authors would like to acknowledge the Medtronic Restorative Therapies Group leadership for financial support of this research. D. Sorensen would like to thank Mr. Brandon Van Leer and Dr. Jan Ringnalda of Thermo Fisher Scientific for helpful sample preparation advice, Mr. Brian Leigh of Medtronic for performing the ICP–OES analysis, Ms. Elizabeth Rentas of Medtronic for assistance in sample preparation, Dr. Wen Tan of Medtronic for helpful discussion related to process–properties relationships, and Ms. Margaret Flury of Medtronic for careful proofreading of this manuscript. We would also like to thank Dr. Ryan Wu formerly of the Mkhoyan Group at the University of Minnesota for invaluable assistance with the monochromated EELS experiments. Finally, WZ acknowledges the support from the Ohio State University Simulation Innovation and Modeling Center (SIMCenter) and Ms. Ying Lu for helpful discussion on finite element modeling. Parts of this work were carried out in the Characterization Facility, University of Minnesota, which receives partial support from NSF through the MRSEC program.

Compliance with ethical standards

Conflict of interest The authors declare that they have no conflicts of interest.

References

[1] Fries RC (2000) Handbook of medical device design. Taylor & Francis, Routledge

[2] Ratner BD, Hoffman AS, Schoen FJ, Lemons JE (2004) Biomaterials science: an introduction to materials in medicine. Elsevier Science, Amsterdam

[3] Joseph RD, ASM International (2003) Handbook of materials for medical devices. ASM International, Geauga

[4] David SA, Babu SS, Vitek JM (2003) Welding: solidification and microstructure. JOM 55(6):14–20

[5] Kou S (2003) Welding metallurgy. Wiley, Hoboken

[6] Lippold JC (2014) Welding metallurgy and weldability. Wiley, Hoboken

[7] Ferro R, Saccone A (2008) Intermetallic chemistry (pergamon materials series). Elsevier, Amsterdam

[8] Iijima M, Brantley WA, Yuasa T, Kawashima I, Mizoguchi I (2008) Joining characteristics of β-titanium wires with

electrical resistance welding. J Biomed Mater Res B Appl Biomater 85B(2):378–384

[9] Chen Z (2007) Joint formation mechanism and strength in resistance microwelding of 316L stainless steel to Pt wire. J Mater Sci 42(14):5756–5765. https://doi.org/10.1007/s10853-006-0671-x

[10] Huang YD, Pequegnat A, Feng JC, Khan MI, Zhou Y (2011) Resistance microwelding of crossed Pt–10Ir and 316 LVM stainless steel wires. Sci Technol Weld Join 16(7):648–656

[11] Fukumoto S, Chen Z, Zhou Y (2005) Interfacial phenomena and joint strength in resistance microwelding of crossed Au-plated Ni wires. Metall Mater Trans A 36(10):2717–2724

[12] Fukumoto S, Tsubakino H, Zhou Y (2006) Heat input and deformation control in resistance microwelding of fine nickel wires. Weld Int 20(9):692–697

[13] Fukumoto S, Fujiwara K, Toji S, Yamamoto A (2008) Small-scale resistance spot welding of austenitic stainless steels. Mater Sci Eng, A 492(1–2):243–249

[14] Waterstrat RM, Giessen BC (1985) The niobium (columbium)-platinum constitution diagram. Metall Trans A 16(11):1943–1949

[15] Eisenbarth E, Velten D, Müller M, Thull R, Breme J (2004) Biocompatibility of β-stabilizing elements of titanium alloys. Biomaterials 25(26):5705–5713

[16] Matsuno H, Yokoyama A, Watari F, Uo M, Kawasaki T (2001) Biocompatibility and osteogenesis of refractory metal implants, titanium, hafnium, niobium, tantalum and rhenium. Biomaterials 22(11):1253–1262

[17] Yuen TGH, Agnew WF, Bullara LA (1987) Tissue response to potential neuroprosthetic materials implanted subdurally. Biomaterials 8(2):138–141

[18] Vander Voort G (1999) Metallography, principles and practice. ASM International, Materials Park, Ohio

[19] Lu Y, Peer AJ, Abke T, Kimchi M, Zhang W (2018) Sub-critical heat affected zone softening in hot-stamped boron steel during resistance spot welding. Mater Des 155:170–184

[20] Amada Miyachi Technical Applications Brief (2000) The effects of polarity on the resistance welding process, vol 3(2), May 2000/rev. December 2015, http://www.amadamiyachi.com

[21] Hernandez AE, Roca AS, Fals HC, Ferraresi VA, Vilarinho LO (2016) Influence of polarity on mechanical properties of dissimilar resistance spot welds f DP 600/AISI 304 steels. Sci Technol Weld Join 21(8):607–613

[22] Harman TC, Honig JM (1967) Thermoelectric and thermomagnetic effects and applications (Lincoln Laboratory publications). McGraw-Hill, New York

[23] Overlooked fundamentals of resistance welding. In: Cieslak MJ (ed) The metal science of joining: proceedings of a symposium sponsored by the TMS solidification committee/MDMD and the physical metallurgy committee/SMD. This symposium was held october 20–24, 1991 at the TMS fall meeting in Cincinnati, Ohio. Minerals, metals and materials society, 1992

[24] Holm R (1999) Electric contacts: theory and applications. Springer, Berlin

[25] Rumble JR (ed) (2018) Thermal and physical properties of pure metals. In: CRC handbook of chemistry and physics, 99th edn. CRC Press/Taylor & Francis, Boca Raton, FL

[26] Pennycook SJ, Nellist PD (2011) Scanning transmission electron microscopy: imaging and analysis. Springer, Berlin

[27] Egerton R (2011) Electron energy-loss spectroscopy in the electron microscope. Springer, Berlin

[28] Fischer-Cripps AC (2011) Nanoindentation (mechanical engineering series). Springer, New York

[29] Hintsala ED, Hangen U, Stauffer DD (2018) High-throughput nanoindentation for statistical and spatial property determination. JOM 70(4):494–503

[30] Johnson KL (1987) Contact mechanics. Cambridge University Press, Cambridge